Scientia Iranica A (2021) 28(6), 2987–3007

SCIENTIA IRANICA

Sharif University of Technology
Scientia Iranica
Transactions A: Civil Engineering
http://scientiairanica.sharif.edu

Numerical modeling of masonry wall under underground waves

A.H. Akhaveissy[a,*], A. Permanoon[a], and R. Raeisi[b]

a. *Department of Civil Engineering, Faculty of Engineering, Razi University, Kermanshah, Iran.*
b. *Department of Civil Engineering, Faculty of Engineering, Bu-Ali Sina University, Hamedan, Iran.*

Received 19 May 2019; received in revised form 9 February 2021; accepted 5 July 2021

KEYWORDS
Underground waves;
Unreinforced masonry walls;
FEM;
Meso scale;
Frictional-cohesive zone material;
Soil-structure interaction.

Abstract. The dynamic behavior of structures has always received considerable attention. The dynamic behavior of structures requires a suitable numerical modeling method to illustrate the behavior of the structure under dynamic loads. In this study, the response of two identical unreinforced masonry walls to the underground blast was examined. The experimental variables were the horizontal distance from the explosion point and the depth in which the explosives were located. After examining the behavior of the masonry walls under high-frequency dynamic loads, different numerical models were applied to simulate the dynamic behavior of these two walls against the underground blast experiments. Thus, several different factors were studied, including the yield criterion, the meso-type and macro-modeling of the masonry wall, and the topography of the site. Finally, due to the degree of accuracy required, it was concluded that each of the methods can be used; however, the most appropriate and accurate modeling method for the unreinforced masonry wall is the frictional-cohesive zone material and modified Mohr-Coulomb model, which provided accurate and precise responses.

1. Introduction

Masonry materials as the oldest building materials have been extensively used in various countries around the world thanks to the ease of construction, high durability, beautiful architecture, and low maintenance costs. In most brick structures, walls are the weakest component due to low ductility and poor shear or flexural strength. Therefore, identifying the behavior of the masonry wall against the incoming loads plays an important role in the design of buildings and the safety of residents. Therefore, various studies have been done on the behavior of the masonry wall under different loads and various types of modeling. Considering brick and mortar use for building materials, Ali and Page [1] presented a nonlinear numerical study of such materials is presented. Dhanasekar et al. [2] introduced a fracture level for masonry material by considering it as a three elliptical member. Taking into account different fracture modes and using three different fracture criteria including Mohr-Coulomb friction law, maximum tensile strain criterion, and maximum compressive stress criterion, Andreaus [3] performed comprehensive research on building materials. Ghiassi et al. [4] proposed an orthotropic macro model for static nonlinear modeling of masonry walls. Grande et al. [5] proposed a new method to determine the

*. *Corresponding author. Tel.: +98 936 8316552*
E-mail addresses: ahakhaveissy@razi.ac.ir (A.H. Akhaveissy); Permanoon.ali@gmail.com (A. Permanoon); Raeisiroya@yahoo.com (R. Raeisi)

doi: 10.24200/sci.2021.53605.3327

nonlinear response by examining unreinforced and FRP-reinforced masonry walls under vertical in-plane and lateral loads. Berardi [6] used the Meso mechanical method to evaluate the onset of cracking and rupture of the masonry wall under in-plane load. Panto et al. [7] used a 3D discrete macro-element model to numerically analyze masonry walls under off-plane loads. Choudhury et al. [8] conducted a numerical and experimental study on a masonry wall. In the study, isotropic elastic damaging 3D modeling and two-step homogenized Finite Element Method (FEM) was used to predict the fracture behavior of masonry wall. Compared with the experimental results, the model is quite accurate. Giambanco et al. [9] modeled the behavior of masonry structures at the interface of mortar and brick by Interface Element Model. A good fit between numerical and experimental modeling was observed for the friction and separation cracks between mortar and bricks. Francesco Parrinello et al. [10] modeled the behavior of masonry structures under cyclic loads using a FEM and a cohesive-frictional interface constitutive model. Akhaveissy [11] modeled the behavior of masonry structures using the DSC/HISS plasticity model and accurately calculated the behavior of the masonry walls, in comparison to the experimental model. Akhaveissy [12] modeled the strength of URM structures using a constitutive model for interface element and predicted the lateral strength of the masonry walls with higher accuracy than FEMA-307 and ATC. Akhaveissy and Milani [13] employed the pushover analysis to analyze the via Martoglio structure (Catania, Italy) using equivalent frame and discrete element and DSC/HISS methods. They also detected the inspected the key and weak links of the structure and suggested strengthening the structure with steel bars. Numerical analysis of the retrofit structure showed that the ultimate strength and ductility were increased by 80% and 70%, respectively. Due to the brittleness of masonry structures, predicting the ultimate strength of masonry structures has always been one of the important issues in the design of such structures. Using the FEM, Deng and Yang [14] numerically examined ECC-retrofitted Confined Masonry (CM) walls and presented a sensitivity analysis of the numerical model of this wall. The masonry wall was tested and numerically examined by Khan et al. [15]. Also, they examined a geosynthetic-reinforced soil wall using 3D modeling on the macro scale. There are different modeling methods for masonry structures, including macro-modeling, Meso-modeling, interface damage, and homogenization methods, which can be used with regard to the concerned accuracy and computational costs. Meso-modeling methods provide more appropriate accuracy than macro modeling methods and one of these two methods should be selected according to the relevant computational cost and accuracy. Karaton and Çanakçi [16] investigated the effect of the meso-model analysis of the masonry wall of the head and bed region of the mortar using the finite element method.

Komurcu and Gedikili [17] investigated the unreinforced masonry shear walls by using the macro and meso modeling. The results show that Meso modeling is very accurate in showing the cracking behavior of the wall. On the other hand, the behavior of structures against dynamic loads has always been a major issue in structural engineering. One of the methods to generate the dynamic load is to use the subsurface explosions of soil by the means of explosives. A subsurface explosion can produce a high-frequency wave, similar to the vibration of the near-field fault [18–20]. In the underground blast like earthquakes, some horizontal and vertical waves are generated (P, S, LOVE, LR); thus, the behavior of structures in the subsurface experiments is in good agreement with the behavior of the structures during a near-field earthquake [21]. Ma et al. [22] examined the damage to the reinforced concrete structures in a subsurface explosion by considering the nonlinear behavior of the structure with two variables, namely the horizontal distance from the explosion center and the structure height by the LS-DYNA software. The behaviors of brittle materials, such as reinforced concrete structures and masonry structures, under dynamic loads have always received attention, and researchers have tried to provide the best method to model the complex behavior of these structures. Therefore, many researchers have examined the behavior of masonry structures and provided retrofitting methods for masonry structures under explosion load. The local damage and fragments of unreinforced masonry walls under close-in explosions were studied experimentally by Shi et al. [23]. Wang et al. [24] investigated the behavior of polymer-retrofitted masonry unit walls under explosion load. In this study, by comparing non-reinforced walls with polymer-retrofitted masonry unit walls, the optimal behavior of the reinforced wall against explosion load was identified. Li et al. [25] investigated the performance of strengthened infill unreinforced masonry walls against blast loads through numerical and experimental study. It is worth mentioning that soil plays a critical role in modeling the structure against dynamic soil loads. Therefore, soil modeling has a significant impact on the results. Researchers are always in pursuit of new ways to model soil. Hu et al. [26] investigated the propagation of blasting waves around underground rock caverns using the 4-D lattice spring model. To analyze wave propagation in soil, Ma et al. [27] compared the capabilities of two soil modeling methods namely finite element modeling in Autodyn software and isotropic continuum damage model. Using Autodyn3D, Hao and Wu [18] investigated soil modeling and the effect of soil type on the propagation of blast waves. In this study, the behavior of masonry structures was investigated under dynamic loads generated by the subsurface explosion. Two experiments with different horizontal spacing and crater depth were performed, and the wall behavior was examined by recording acceleration at different points. The different numerical methods were used to model the masonry wall and soil and the effects of macro and Meso modeling, meshing dimensions, and Wiliam-Warnke and Menetrey-Willam fracture surfaces on brick modeling were examined. Further, the impact of the site topography, the Drucker-Prager elastoplastic failure surface, and soil modified Mohr-Coulomb and Laysmer boundaries were considered to determine the best solution to model the behavior of masonry structures under dynamic load.

2. Mechanical properties of materials and dimensions of experimental samples

2.1. Mechanical properties of masonry wall

The masonry wall was built by bricks and sand/cement mortar. The walls were $1200 \times 960 \times 100$ mm, with a ratio of $h/l = 1.25$. To test the compressive strength of the mortar according to the ASTM c109/c109M standards, $50\times50\times50$ mm cube samples were used [28]. The compressive test of the masonry unit was carried out according to the Australian Standard AS1012.9: 1999. All tests were performed after 29 days of curing (Table 1). In Figure 1, the average compressive strength of each element of the masonry unit is shown. The compression test result was used to estimate the other mechanical properties of the materials by the ACI and ACI530 Standards [29].

(a) (b) (c)

Figure 1. Compressive strength test: (a) Brick, (b) masonry unit, and (c) mortar.

Table 1. Compressive strength of wall components.

Components of masonry wall	Average of compressive strength
Brick	10.5 MPa
Mortar	7.2 MPa
Masonry specimen	8.4 MPa

2.2. Mechanical properties of the soil

A decisive factor in investigating the underground blasts is the mechanical properties of soil. Due to the fast wave transmission in the soil environment, the CU test according to the ASTM D4767 standard [30] was used to obtain soil mechanical properties. As the crater soil is considered to be degraded and does not have any cohesion, the internal friction angle of soil can be calculated via the direct shear test according to the ASTM D3080 standard [31]. For each experiment, three soil samples from the site were used. Figure 2 shows the axial stress-strain diagram of the soil in the triaxial compressive experiment. The strength of the Mohr circle and strength envelope lines of different samples are shown in Figure 2. According to Table 2, the amount of cohesion, internal friction angle, modulus of elasticity, and the Poisson ratio of soil are 0.02, 35, 530, and 0.37 MPa, respectively. According to geological studies, the soil of the region was identified as Glacial till (very dense (Figure 3)). By performing

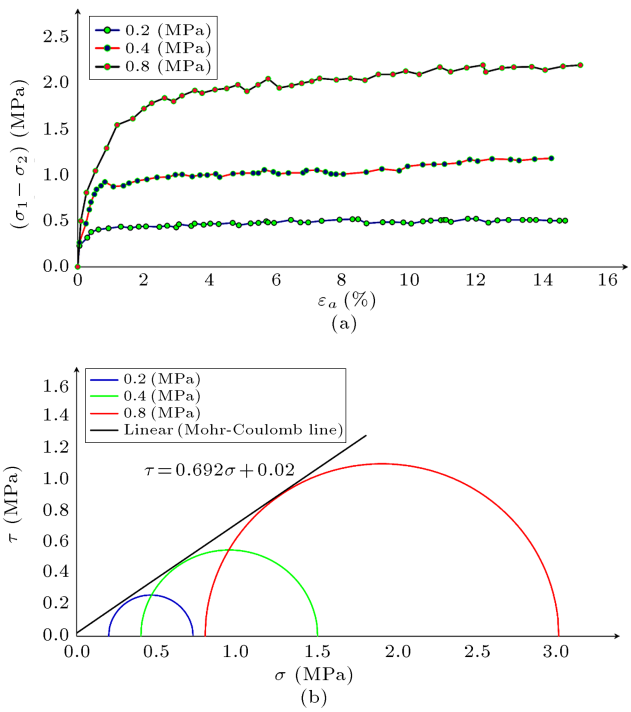

Figure 2. (a) Average of the axial stress-axial strain of soil. (b) Mohr circle and strength envelope lines of soil.

Table 2. Mechanical properties of site soil according to triaxial test.

Properties of glacial till	
C (MPa)	0.02
ϕ (degree)	35°
E (MPa)	530
ν	0.37
e	0.4

Figure 3. View of wall foundations.

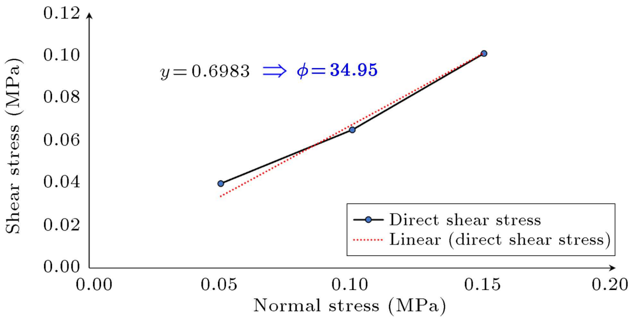

Figure 4. Direct shear test for friction angle of the crater.

the direct shear test for the soil of the crater (crater site), the value of internal friction angle was obtained according to 3 experimental samples 35°(Figure 4).

2.3. Underground blast test

In this study, 2 walls of similar dimensions (1200 × 960 × 100 mm) were tested. The test methods for the two walls were almost the same, the only difference was the amount of explosive used, the depth, and the horizontal distance between the explosive and the wall. In Sample (1), the explosive was placed at a horizontal distance of 3.5 m from the wall and a depth of 1.5 m. For Sample (2), these values were 2 m and 1 m, respectively. The T.N.T values in the first and second experiments were 1.92 kg and 4.9 kg, respectively. Figure 5 shows the dimensions of the samples and the location of the accelerometer sensors with an accuracy of 0.01 g and 50 g power. It should be noted that the horizontal acceleration on the foundation and above the wall and the vertical acceleration above the wall were measured in the first experiment, though, only horizontal acceleration on the foundation and above the wall was recorded in the second experiment. The explosive was placed in UPVC pipes and was completely enclosed using two closures to transfer more energy to the soil. In each of the two experiments, the explosive material was placed

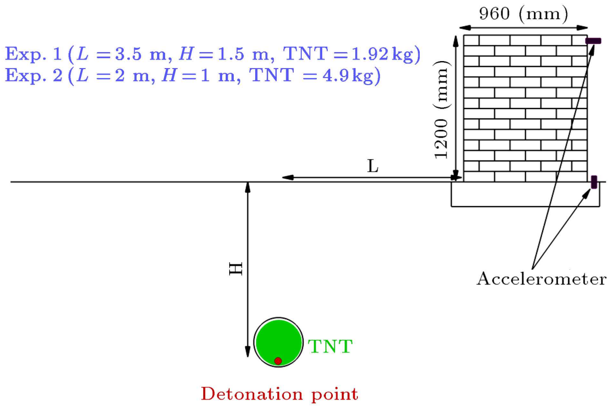

Figure 5. The dimensions of the samples and the location of the accelerometer sensors.

directly along the length of the wall and was covered by the soil of the crater. It is worth noting that in the first experiment, with 1.92 kg TNT, a horizontal distance of 3.5 m from the wall, and a depth of 1.5 m, the wall behavior was almost linear, and no cracks were observed in the wall (Figure 6). After two-times integration from the horizontal time-acceleration curve, the time-displacement curve will result. By using this stage, the maximum absolute displacement of the wall was calculated about 0.7 mm. According to FEMA 356 [32], this value is less than 0.1%, therefore it is in the linear range and has immediate occupancy performance (Figure 7). In the second experiment, the amount of the explosives increased and the position of the explosives was closer to the masonry wall, and the cracks and fractures appeared in the fourth-bed joint row of the mortar of the masonry wall. The results showed that when the vertical wave approached, the wall moved upward slightly, and when the horizontal wave approached, the wall was impacted by the shear wave shock and fractured at the joint of the fourth bed (Figure 8). The response of recorded time-acceleration to two masonry wall samples is shown in Figure 9. As shown in Figure 9(b), the axis marked in the figure is from 0.13 s to 0.25 s. This figure shows the time of failure of the wall. In numerical analysis, this section has been discarded.

3. Finite element modeling in different ways

To obtain the most appropriate numerical modeling method, all effective parameters such as soil criterion, far-field boundaries to prevent wave reflection, modeling of the masonry wall, the topography of the site, and dynamic loading imposed by the explosion of the explosives were included. Hence, a stepped logical process was adopted to find the most suitable numerical response that is close to the experimental results. Since the dynamic load power was greater in the second experiment, the masonry wall was fractured

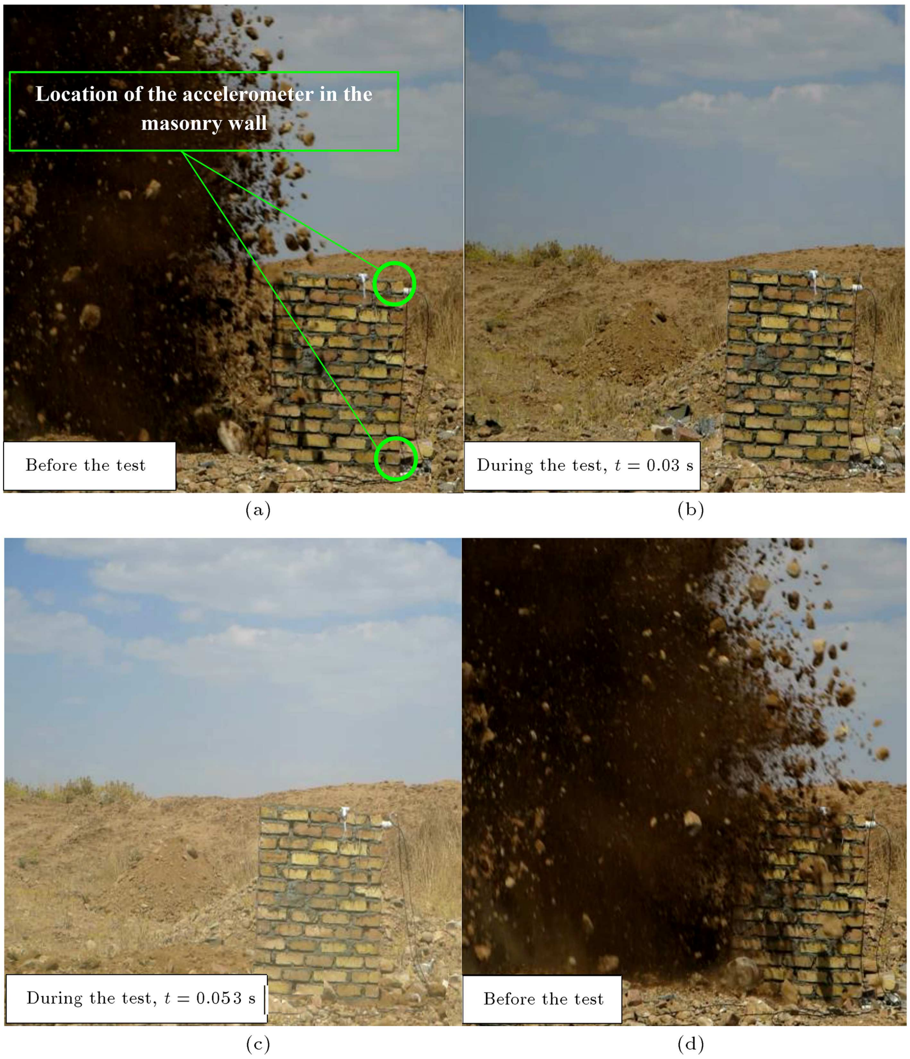

Figure 6. The first experiment: (a) Before the test, (b) during the test, $t = 0.03$, (c) during the test, $t = 0.053$, and (d) after the test.

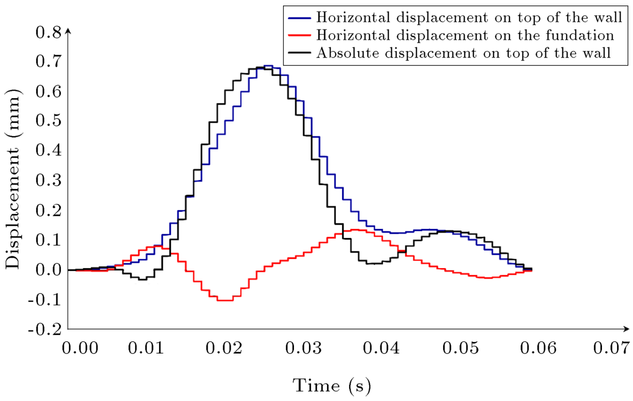

Figure 7. Absolute horizontal displacement on top of the wall in the first experimental.

and damaged in the fourth-bed joint row of the mortar; hence, the second experiment results were used to compare the numerical method using Ansys Software and experimental data.

3.1. The fixed parameter in all of the models

3.1.1. Boundaries

Boundaries play a determining role in numerical analysis. In this section, the effect of far-field boundaries is examined by considering a simple example. In the dynamic modeling of explosions and earthquakes in the soil environment, the size and artificial boundary of the finite element model can usually effectively determine the dynamic response and wave attenuation in the finite element environment. Selecting the fixed or free boundary condition reflects the input wave into the model. This reflection interferes with the input wave and makes it very difficult to analyze the results. Therefore, absorbent boundaries are necessary. A set of non-reflection boundary conditions was proposed. For example, to understand how the non-reflection boundary works, viscous boundary element [33], strip element [34], and infinite element [35] are included in FEM. These methods can be applied to other types of numerical methods. For instance, viscous bound-

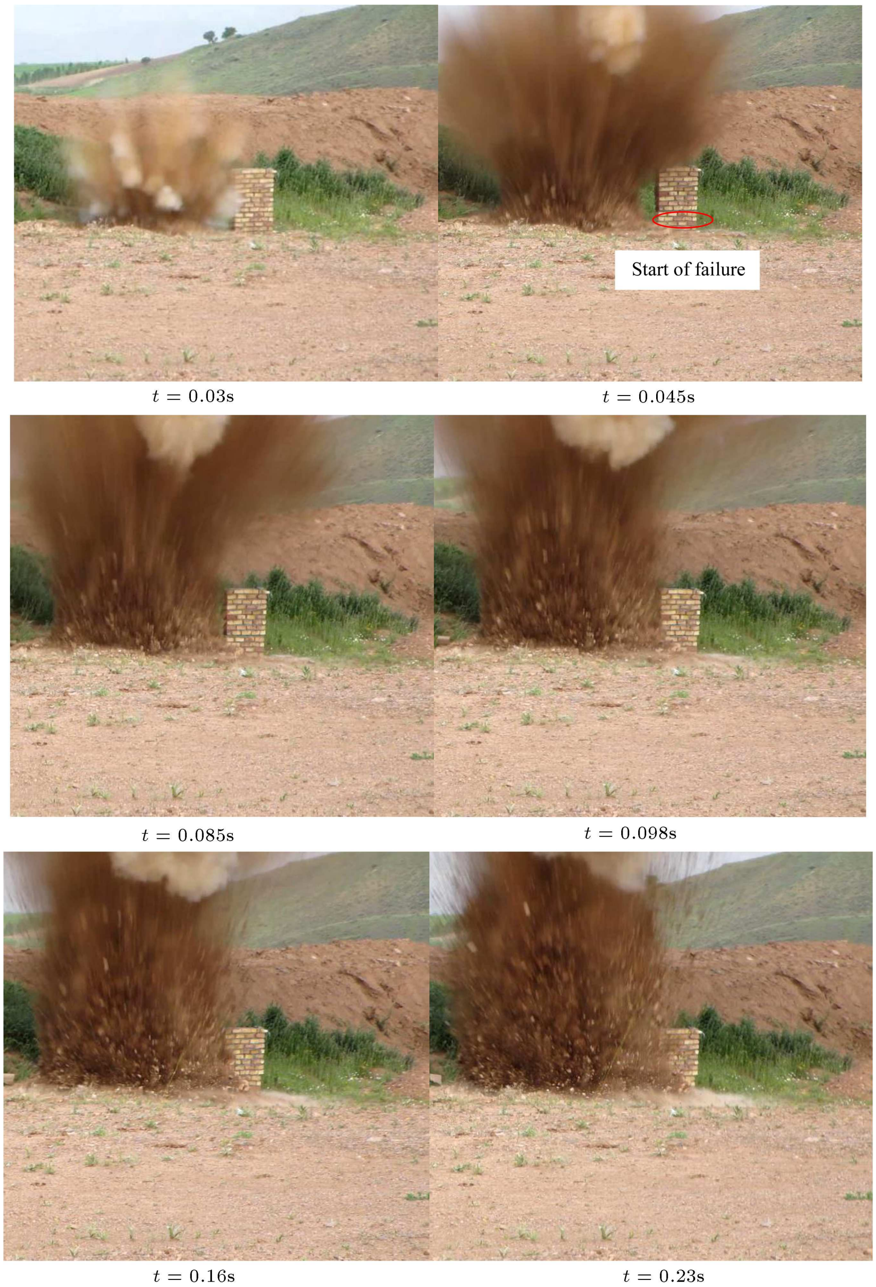

Figure 8. A few frames of the second experiment and the wall fracture in the fourth-bed joint row.

ary element was utilized in Discrete Element Method (DEM) [36] and Discontinuous Deformation Analysis (DDA) [37]. In this research, a viscous boundary element was used. For this method, the normal and shear viscous tractions are given as Eq. (1):

$$t_n = -\rho \bar{A} C_p a, \qquad t_{s1,s2} = -\rho \bar{A} C_s b,$$

$$a = \frac{8}{15\pi}(5 + 2S - 2S^2), \qquad b = \frac{8}{15\pi}(3 + 2S),$$

$$S = \sqrt{\frac{(1-2\upsilon)}{2(1-\upsilon)}},$$

$$C_s = \sqrt{\frac{G}{\rho}}, \qquad C_p = \sqrt{\frac{E(1-\upsilon)}{(1+\upsilon)(1-2\upsilon)\rho}}, \tag{1}$$

where, ρ is mass density $\bar{A}$ is the equivalent site, C_p and C_s, respectively, are the P-wave and S-wave velocities, a and b are the dimensionless parameters, G is shear modulus, υ is Poisson ratio. In the numerical model, to investigate the effect of boundary conditions, wave propagation was studied via one-dimensional modeling. The mechanical specifications (Table 1) were used. The numerical model was considered to be two-dimensional, with a length of 10 m in the longitudinal direction (X) and a length of 1 m in the transverse direction (Y),

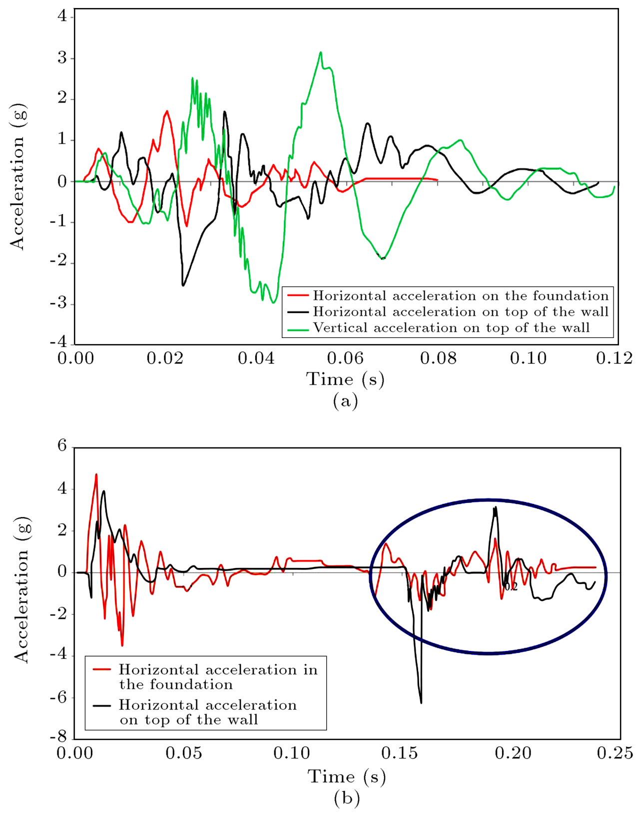

Figure 9. Recorded time-acceleration results: (a) The first experiment and (b) the second experiment.

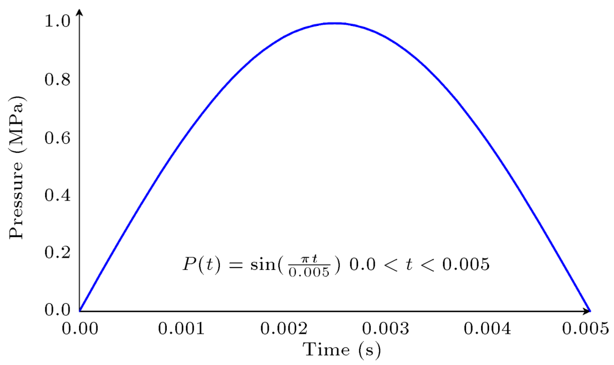

Figure 10. Input dynamic pressure.

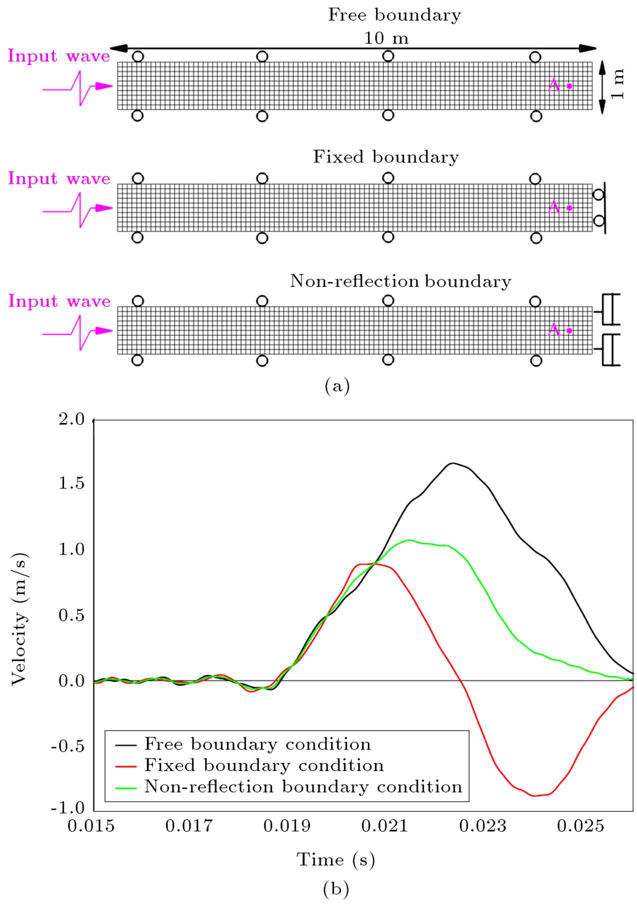

Figure 11. Comparison of three kinds of boundary conditions: (a) Dimension and meshing of Finite Element Method (FEM) and (b) wave propagations detected at three measure points A.

with three different boundary conditions. The input wave was applied to the left side of the model as a dynamic pressure as shown in Figure 10. At point A, the velocity value was checked for three different conditions. The coordinates of point A are $x = 9500$, and $y = 500$ mm. As indicated in Figure 11, the numerical results of the three measurement points identified in the above models are summed together and then compared. Regardless of the damping effect, there exists a negative wave velocity in the vicinity of the right side of the boundary when the right boundary of the model is a fixed boundary condition. This state indicates that the input wave reflects on the right boundary and propagates along the negative z-axis. In some cases, the right boundary of the model is a free boundary condition. Accordingly, when the incident wave reaches the right boundary site, the wave velocity rises sharply, therefore, there is a tendency for the incident wave and the reflected wave to superimpose. When the right boundary of the model is a non-reflection boundary condition, no clear change can be observed in the wave shape located at the right boundary site in comparison to the incident wave. Therefore, it could be said that the artificial boundary does not affect wave propagation. According to the numerical results, the implementation of non-reflection boundary conditions could be effective. In the models under discussion, the soil zone of all numerical models is considered as the semicircle and in all models, radius of the semicircle is 1500 mm. Regarding the velocity of S and P waves, the required time for the wave to reach the far-field boundaries is 0.046 and 0.022, respectively. Accordingly, the return wave from the S wave does not affect the behavior of the wall. At far-field boundaries, the P-wave interference was reduced due to the non-reflected boundaries. The combine 14 element was used to model the non-reflected boundaries. This

3D element considers linear behavior and dumping coefficient.

3.1.2. Blasting load

To apply the pressure equivalent to the explosion of the explosive TNT, Eq. (2) was used, which was applied on the crater internal dimensions. In this equation, P_0 is the maximum amount of pressure imposed by the explosion of explosives, and t_a is the time when the wave resulting from the explosion reaches the structure. According to the equation provided by the US Army Code (TM5-855-1) [38,39], the value of P_0 in the underground blast is determined as follows:

$$P_t = P_0 e^{\frac{t}{t_a}},$$

$$P_0 = 48.8\rho c f_c \left(\frac{2.52R}{W^{\frac{1}{3}}}\right)^{-n}, \tag{2}$$

where ρ represents the mass density, c is the average velocity of wave propagation in soil, R is the distance from the structure to the explosion center, and W represents the weight of the explosives. All values were calculated according to the aforementioned US Army Code (TM5-855-1) and applied to the crater.

3.1.3. Numerical method

In this section, the FEM was compared with other numerical methods to ensure that this method can simulate underground blasts (high-velocity dynamic behavior). The following example [40] was considered to compare the results of the FEM with other methods. This experimental model has been studied by some researchers and analyzed through different numerical methods [41,26,27]. The dimensions of the experimental model and the location of the blast load are shown in Figure 12. For the numerical modeling of this example, 4-node 2-dimensional elements were used. In far-field boundaries, non-reflection boundaries were used to minimize the effect of reflection and wave

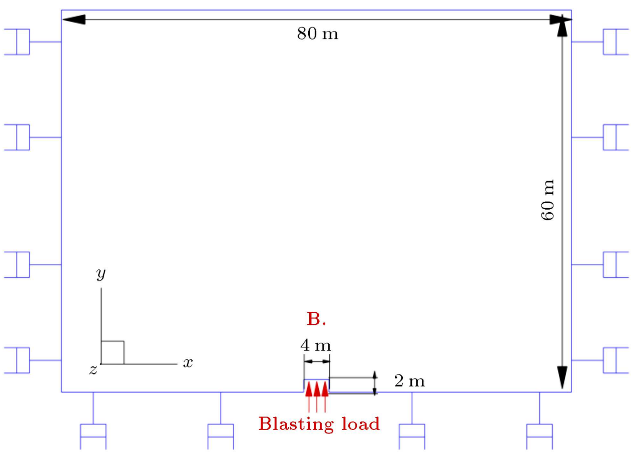

Figure 12. The dimensions of the experimental model and the location of the blast load [40].

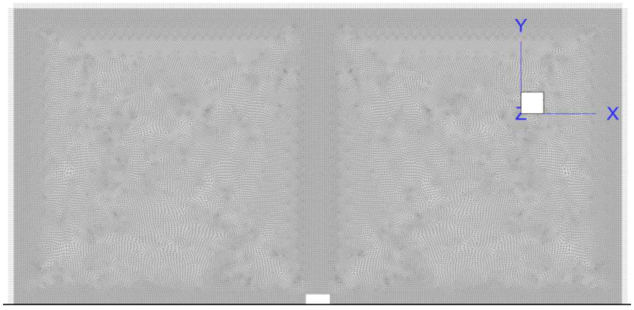

Figure 13. The numerical model meshing.

interference. Figure 13 shows the numerical model mesh using the FEM (current study). Through the analysis and comparison of the results, it is found that the FEM has good consistency with other underground blasting modeling methods. Figure 14 shows the propagation of the wave in the environment at different times. These results are in good agreement with Ref. [26]. As shown in Figure 15, by examining the wave velocity at point B (8 m above the blast point), it is revealed that the FEM has good accuracy for modeling the underground blasts. In what follows, to ensure the validity of the results of the FEM, the experimental model under discussion is examined using different numerical models. Therefore, to provide a proper model for investigating the behavior of a brick wall under dynamic load, the finite element method is used.

3.2. Model (1)

Features of the Model (1):

(a) The masonry wall was modeled using macro modeling;

(b) Soil geometry was considered and the site topography was not considered;

(c) The failure surface classic Drucker-Prager was used for soil.

In this method, the wall was modeled as a macro and the size of each element was approximately 30 mm (Figure 16). In other words, by using the mechanical properties of the unit, the entire wall behavior was considered the same as the masonry unit. Further, Wiliam-Warnke failure surface [42] was used to investigate the nonlinear behavior of the masonry wall. This failure surface includes cracking in tension and crushing in compression. The values of compressive and tensile strengths of the masonry unit were set to be 8.4 MPa and 0.4 MPa according to the experimental results (Figure 16). The values of the input parameters of William Warnke's failure surface were entered according to William Warnke's recommendation [42]. The numerical model of the wall with Solid65 element with 30 mm dimensions was free-meshed. The soil was modeled as a semicircle with a radius of 15000 mm centered on the explosions site (crater). The waves

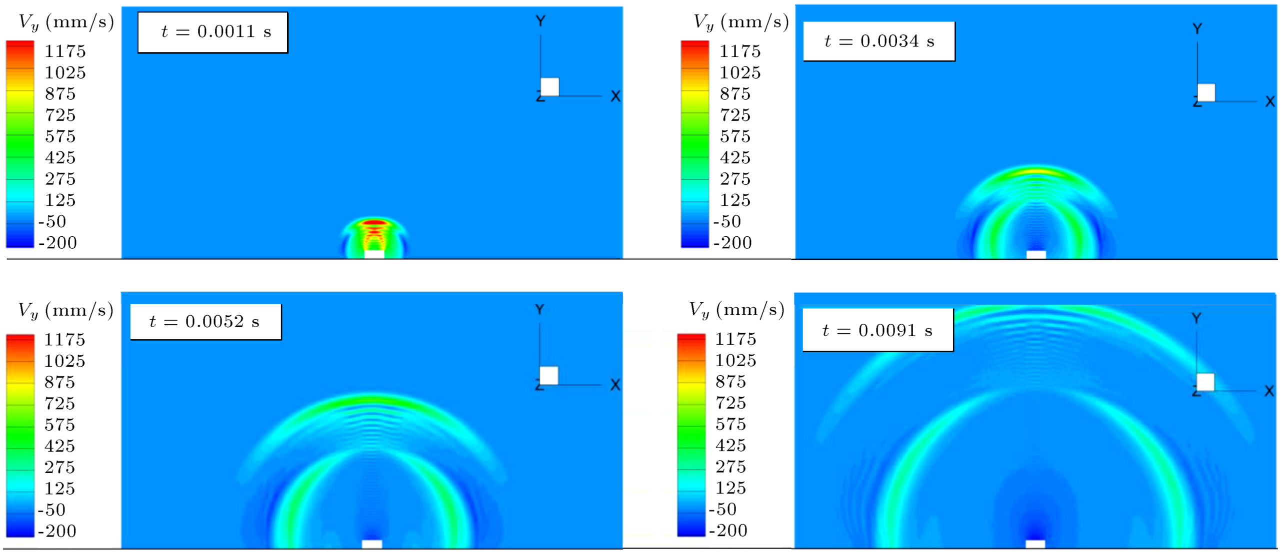

Figure 14. Wave propagation in the soil at different times.

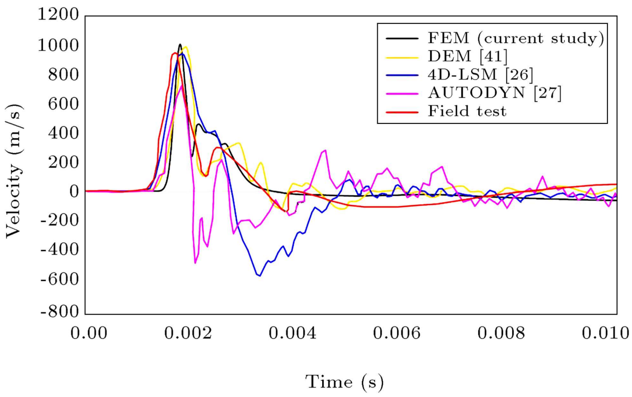

Figure 15. Comparison of finite element method and other numerical methods.

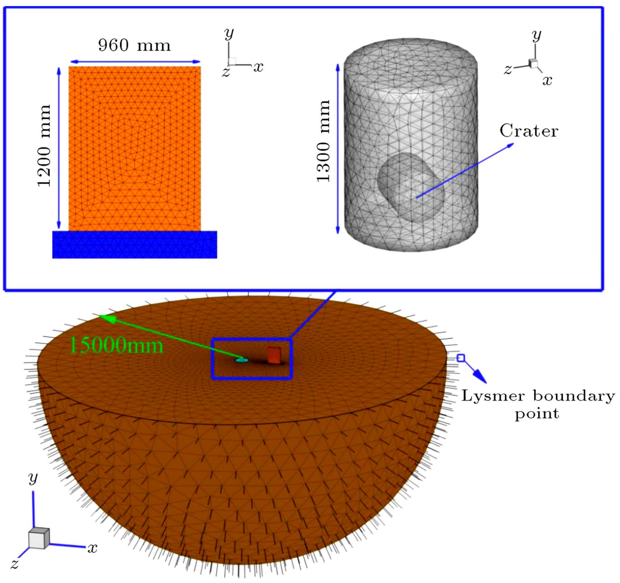

Figure 16. A schematic view of the finite element model, wall meshing, soil zone, and crater.

were prevented from reflecting by increasing the soil dimensions. The soil with solid65 element near the crater and the wall with smart size 2 were free-meshed, and the dimensions of the mesh increased from the center of the model. For the nonlinear behavior of soil, the classic Drucker-Prager model was used. Through dynamic analysis of the problem of Model (1), it is found that the maximum values of ground acceleration were almost the same in numerical and experimental models (Figure 17(a)). However, the frequency of the numerical model has disappeared, which is probably caused by not considering the topography of the site. Also, by comparing the horizontal acceleration of the top of the wall with experimental results, it is found that the maximum acceleration response was relatively close to each other in the numerical and experimental models; however, due to the growth of cracking in the elements and its continuity, the William-Warnke yield surface could not consider the dynamic behavior of the model correctly after cracking (Figure 18). In this model, the shear transfer coefficient of the open crack (β_t) was about 0.3 and it was about 0.7–0.9 (β_c) when the open crack was closed under the effect of the structural behavior [43]. Since the value of the shear transfer coefficient drops sharply during multiple crack closing and opening cycles less shear is transferred between two surfaces. William Warnke failure surface cannot decrease the shear transfer coefficient (Figure 17(b)). The reflected wave at the far-field boundary is investigated and the magnitude of the force reaching the Lysmer boundary element is shown in Figure 19(a). At time 0.025 s, the wave caused by applying the pressure on the crater has reached the far boundaries in the numerical model. If this wave can be noticed after colliding the boundary and returning to the original point, the wall, then there

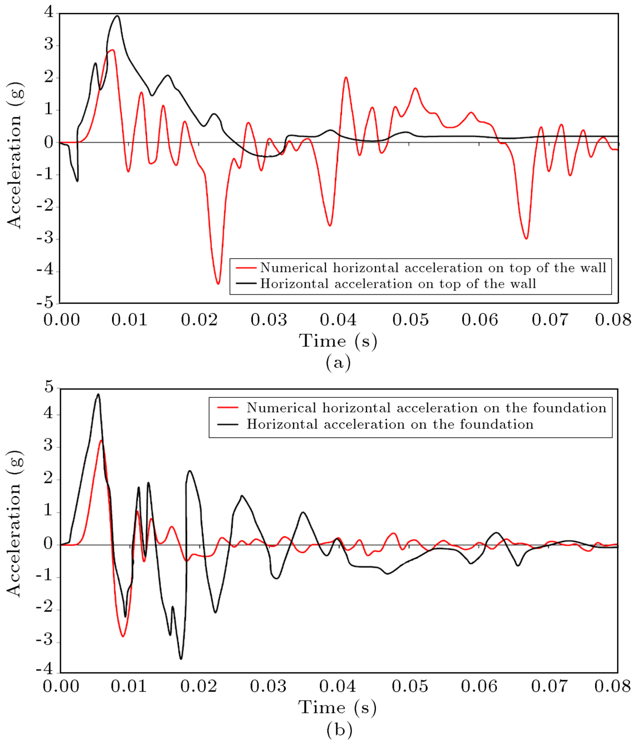

Figure 17. Comparison of the time-acceleration graph: (a) Above the wall, and (b) on the foundation.

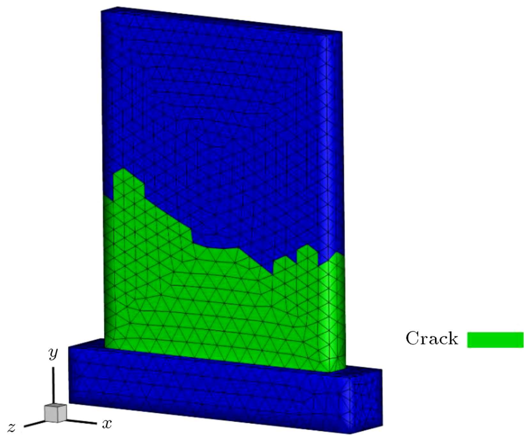

Figure 18. Cracking pattern of brick wall with free meshing at the end of the analysis.

would be an oscillation at 0.05 s in the response to the acceleration on the foundation. As it can be observed in Figure 19(b), there is no obvious wave returning to the system. To prove this claim, the model was analyzed without Lysmer boundary elements (Figure 19(b)), and it was revealed that the wave has returned to its original point at 0.05 s, implying that the wave recurrence has taken place. Therefore, it can be said that the boundary elements have been very effective. Therefore, it is important to consider the modeling of far-distance and absorbing boundaries and the radius of the soil zone in numerical modeling to achieve an appropriate response.

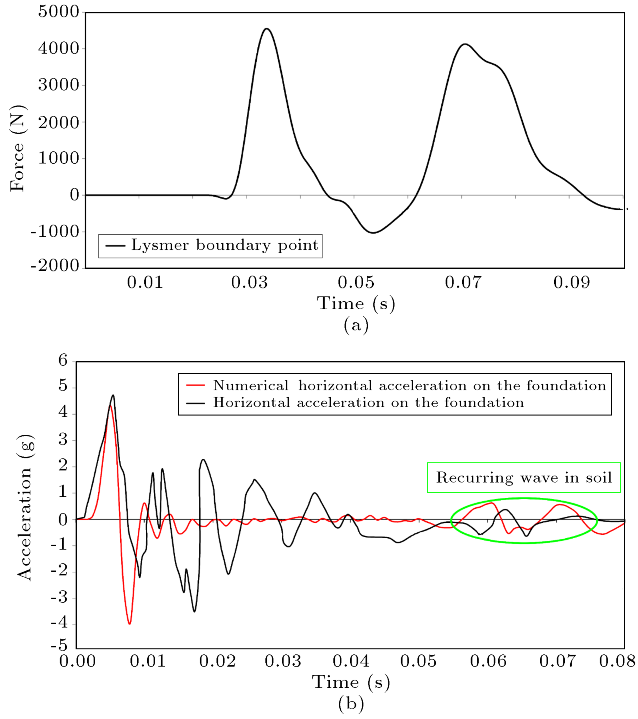

Figure 19. (a) Force of an element on Lysmer boundary specified in Figure 5 and (b) time-acceleration on the foundation without Lysmer boundary.

3.3. Model (2)

Features of the Model (2):

(a) The masonry wall was modeled using macro modeling and meshing size as large as a brick;

(b) Soil geometry was considered without topography of the site;

(c) The failure surface classic Drucker-Prager was used for soil.

In this model, compared with the Model (1), the soil modeling parameters are fixed. As observed in the previous model, due to the expansion of the cracks and their continuity in the elements of the masonry wall, the fractures progressed in most parts of the wall. This implies that the wall behavior was far away from reality. Therefore, the dimensions of the elements (meshing) were changed in this model, and the size of each element was considered to be approximately equal to that of a brick. This decision was made according to the results of the behavior of the wall under dynamic loads since experimental Model 2 was fractured at the mortar. As a result, the size of each wall element was modeled like a brick, so that the *Gaussian* points were almost close to the actual mortar location. This allows elements entering the plastic region to be collapsed according to the position of the wall Gaussian points with respect to this region [13,44–46]. The meshing and crack pattern is shown

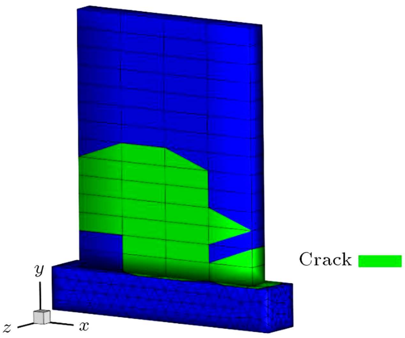

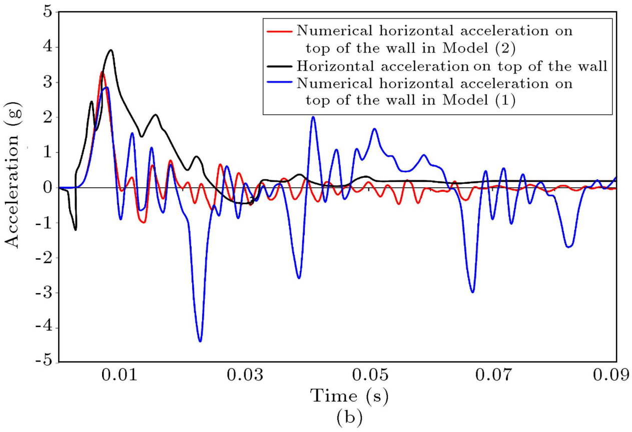

Figure 20. (a) Meshing and cracked patterns at the end of the analysis. (b) Comparison of the time-acceleration of Model (2), Model (1), and experimental model.

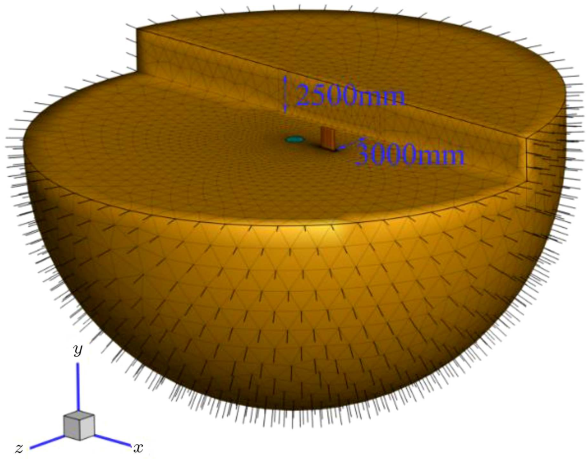

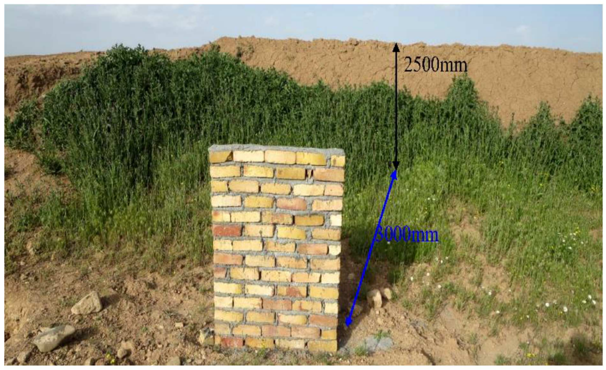

Figure 21. (a) A schematic of the numerical model. (b) Experimental model and site topography.

in Figure 20(a). In Figure 20(b) the results of the examination of the horizontal acceleration above the wall clearly show that by increasing the size of the elements, the numerical results become more consistent with the experimental results. Given that the *Gaussian* points of each element in the experiment were close to the actual location of the mortar, it can be claimed that more consistency with experimental results is achieved.

3.4. Models (3) and (4)

Features of Model (3):

(a) The masonry wall was modeled using macro modeling and meshing size which was as large as a brick;

(b) Soil geometry was considered together with the topography of the site;

(c) The failure surface-classic Drucker-Prager was used for soil.

Features of the Model (4):

(a) The masonry wall was modeled using macro modeling and meshing size which was as large as a brick;

(b) Soil geometry was considered together with the topography of the site;

(c) The failure surface-modified Mohr-Coulomb was used for soil.

Therefore, there is a difference between the acceleration on the foundation resulting from the numerical analysis in this model and the experimental results, it seems unlikely to expect the numerical responses to be close to the experimental result by ignoring the site topology. In this model, the natural complications of the site were generally modeled to examine the impact of the topography of the site. In the second experiment, there was an embankment at a distance of about 3 m back of the wall with an average height of 2.5 m. In this model, without considering minor variations of natural complications, the embankment was uniformly modeled with a distance of 3 m from the wall and a height of 2.5 m. The effect of the site topography was investigated, as shown in Figure 21. Numerical analysis fully revealed the effect of topography and regional complications on the numerical responses. Numerical analysis fully revealed the effect of terrain and regional complexity on the numerical response. The maximum acceleration value on the foundation was in good agreement with several initial oscillations. These appropriate numerical

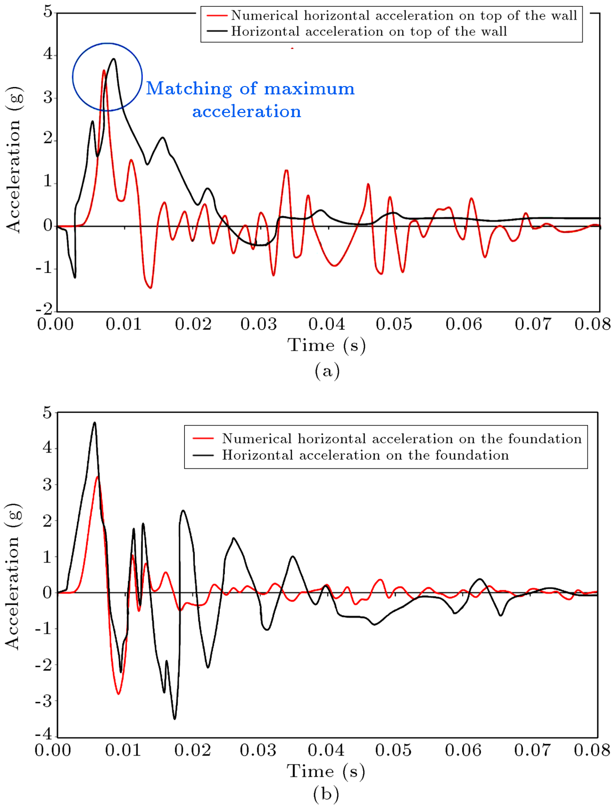

Figure 22. Comparison of time-acceleration of Model (3) and experimental model: (a) Top of the wall and (b) on the foundation.

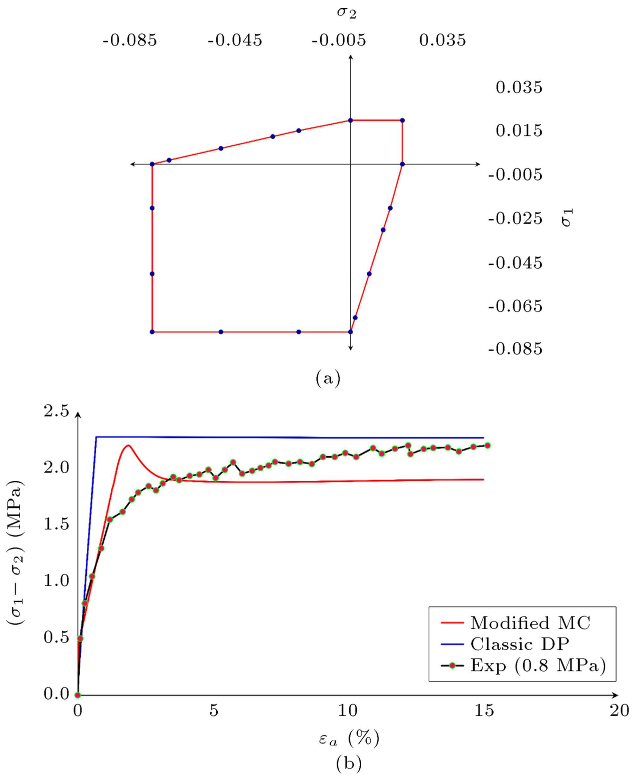

Figure 23. (a) Modified Mohr-Coulomb in the 2D stress space and (b) comparison of the criterion of classic DP and modified MC with triaxial experiment (confining pressure is 0.8 MPa).

responses to the soil resulted in an increase in the maximum acceleration above the wall (Figure 22(b)). Further, given that the Drucker-Prager classic yield surface determines its yield criterion based on initial C and ϕ (elasto-plastic), this behavior is likely to be far from reality. In the following model, the modified Mohr-Coulomb yield criterion [47] was used, to allow for better behavior in soil modeling. This yield surface models the soil behavior of two yield surfaces, that is, it defines the yield criterion after the first yield based on residual strength parameters C', ϕ'. The following equation is established for its strength parameters:

$$\frac{C}{\tan\phi} < \frac{C'}{\tan\phi'}. \tag{3}$$

Following the first yield, the residual strength is 80% of the initial strength [48]. The input values of the mechanical parameters for the modified Mohr-Coulomb yield criterion are shown in Table 3. Figure 23(a) shows the yield surface of the modified Mohr-Coulomb in the 2D stress space according to the soil characteristics of the test site. To ensure the accuracy of the finite element results, the triaxial experiment was modeled under confining pressure of 0.8 MPa. Figure 23(b) shows the results of the numerical modeling of the triaxial experiment obtained through the classic Drucker-Prager yield criterion and the modified Moher-Coulomb. It is clear that the results of the modified Mohr-Coulomb are close to the experimental results and have almost greater potential to model the soil. Model (4) is a combination of Model (3) and the modified soil Mohr-Coulomb yield surface. Therefore, by comparing the response of the acceleration on the foundation in numerical and experimental models

Table 3. Input parameters of modified Mohr-Coulomb yield criterion.

Property of Mohr-Coulomb	Soil	Crater
Initial inner friction angle (ϕ)	35	33.95
Initial cohesion (C)	0.02	0
Dilatancy angle (ψ)	35	35
Residual inner friction angle (ϕ')	0.8×35	0.8×33.95
Residual cohesion (C')	0.8×0.02	0

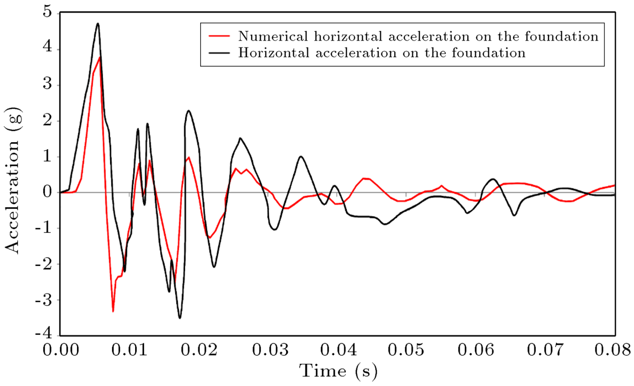

Figure 24. Comparison of the time-acceleration graphs of the Model (4) and the experimental model.

(Figure 24), it can be found that this failure surface can model the soil behavior better than Drucker-Prager classic yield surface under dynamic load. Hence, this numerical failure surface can be considered as a proper failure surface for soil modeling under dynamic and static loads. Accordingly, in this study, the parameters of the soil model are considered to be fixed.

3.5. Model (5)

Features of Model (5):

(a) The masonry wall was modeled using Meso modeling with cohesive-frictional interface;

(b) Soil geometry was considered together with the topography of the site;

(c) The failure surface-modified Mohr-Coulomb was used for soil.

In this model, a Meso modeling method with frictional-cohesive zone material was used for numerical modeling of the wall. This method is more accurate than the macro method and has a higher computational cost than the previous model. The fracture is probable for both conditions where separate brick and mortar modeling are considered, and there is a possibility of failure and sliding for any part of the masonry unit that is susceptible to failure in terms of strength. In this part, the failure surface of Menetrey-Willam [49] was used to investigate the nonlinear behavior of bricks, and the friction-cohesion zone material method was used to simulate the behavior of mortar. The bricks were modeled in 3D using Solid185, and each node had three degrees of freedom. The contact and target elements were used to model the mortar by considering the behavior of the cohesive zone. This model can model the brittle behavior of the masonry wall and the separation and sliding of bricks according to the first and second fracture modes [50–53]. As illustrated in Figure 25, the schematic diagram shows the Meso method for modeling masonry units. Since the brick shows a brittle behavior like concrete, the Menetrey-Willam [49] yield

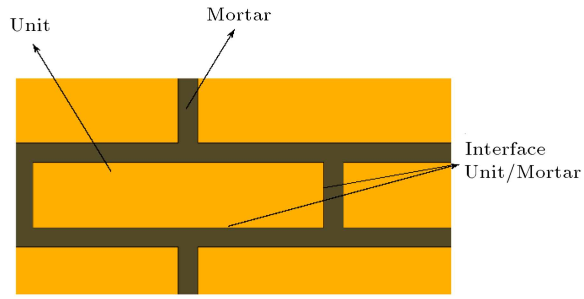

Figure 25. Details of the meso method.

criterion was used to model the nonlinear behavior of the brick. The failure surface can simulate brittle behavior relating to tensile and compression softening. The general form of the nonlinear behavior of tension and compression is similar to Figure 26. The Cohesive Zone Material (CZM) model was used for investigating the behavior of the mortar as the interface. This method is based on the relationship between tension and separation. To introduce the mortar as an interface between the bricks, the CZM method with the contact element was used which includes friction in addition to tension and separation. The CMZ behavior is introduced based on Figure 27. Given that debonding has been considered in both the normal and shear components, the Mixed-Mode Debonding was used to introduce CMZ. The normal and tangential stiffness values were calculated according to Eq. (4):

$$k_n = \frac{E_b E_m}{h(E_b - E_m)}, \quad k_t = \frac{G_b G_m}{h(G_b - G_m)}. \tag{4}$$

In addition, the fracture threshold is based on the power form (Eq. (5)). When determining the friction between the contact surfaces where debonding occurred, the tangential stress is calculated as the maximum value between the tangential stresses governed by the debonding model, and the tangential stress is governed by the friction law.

$$\left(\frac{G_n}{G_{cn}}\right)^2 + \left(\frac{G_t}{G_{ct}}\right)^2 = 1, \qquad G_n = \int P du_n,$$

$$G_n = \int \tau du_t. \tag{5}$$

Since the nature of the underground blasting wave is dynamic, it is evident that the dynamic friction coefficient is decreasing as a result of decreasing friction between particles with a steepness relative to the static friction coefficient. This reduction is considered in the ANSYS software by Eq. (6):

$$\mu = MU \times (1 + (FACT - 1)\exp(-DC \times V_{rel})). \tag{6}$$

3.5.1. Numerical modeling and calibration of model CZM parameters

To calibrate the input parameters of Model (5), ex-

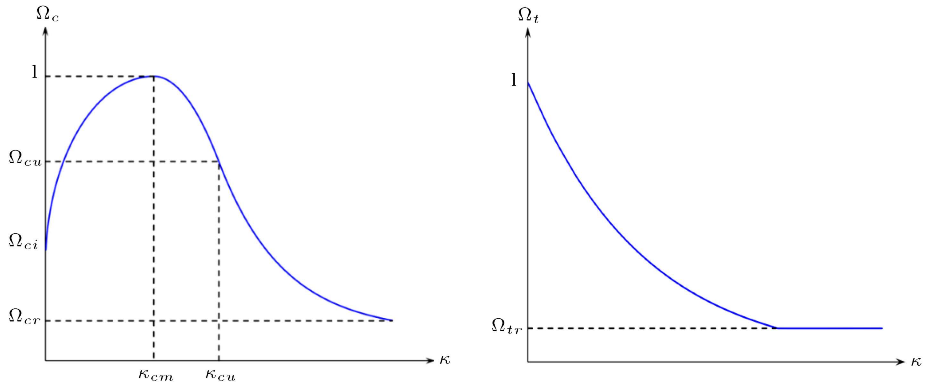

(a) Compression (b) Tension

Figure 26. Brick behavior model in tension and compression.

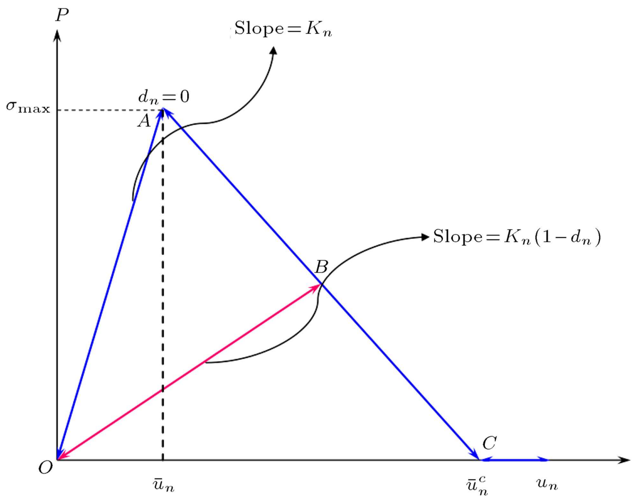

Figure 27. The behavior of interface element using stress-separation.

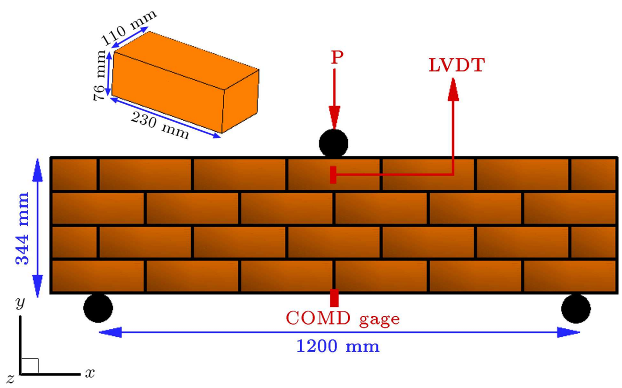

Figure 28. Dimensions of Chimoon and Attard [10] experimental model and how to apply the load.

perimental data should be used. Since the pressure test was conducted only for the mortar and given that the compressive strength of the mortar used in the construction of the wall was close to the strength value of the mortar used in the Chaimoon three-point test [10], the strength parameters measured in the experimental data by Chaimoon was used to model the wall in this study. Therefore, the Chaimoon test was used to test the parameters of the behavioral model with the frictional-cohesive zone material. Three-point flexural test which was tested by Chaimoon and Attard [10] is shown in Figure 28. In this section, the bricks behavior was considered to be linear due to its high compressive strength, and the input coefficients were calculated according to Table 4 to model the mortar behavior (Table 5). To compare Meso and macro methods, Chaimoon and Attard [10] experiment was modeled using both Meso and macro methods. In macro modeling, the compressive and elastic strength of the mortar was used for numerical modeling. It seems logical to use the mechanical properties of the mortar as equivalent to the mechanical properties of the masonry unit since the brick strength is extremely high and the mortar has fractured. Hence, the mechanical properties of the mortar were considered in macro modeling. Figure 29 shows the meshing in Meso and macro methods. The comparison of the fracture modes in Meso, macro, and experimental models reveals that the Meso model has a high potential to model the complex behavior of brick walls Figure 30(a) and (b); however, given that the initial stiffness is well simulated in the macro modeling, it behaved almost

Table 4. Measured strength parameters of materials by Chimoon and Attard [10].

Masonry unit	**Dimensions**	***E*** **(MPa)**	ν	f_C **(MPa)**	f_t **(MPa)**	f_b **(MPa)**	G_f^I **(N/mm)**	G_f^{II} **(N/mm)**
Brick	$76 * 230 * 110$	17500	0.15	31.13	–	–	–	0.564–2.436
Joint	10 mm	3360	0.2	7.26	0.086	1.2 f_c	0.002	0.037

Table 5. Frictional-cohesive zone material coefficients.

Property of frictional-cohesive zone material	
Maximum normal contact stress ($\sigma_{\max}$)	0.135
The critical fracture energy density (energy/site) for normal separation (G_{cn})	0.002
Maximum equivalent tangential contact stress ($\tau_{\max}$)	0.18
The critical fracture energy density (energy/site) for tangential slip (G_{ct})	0.037
Artificial damping coefficient (η)	0.998
Flag for tangential slip under compressive normal contact stress (β)	1
Normal contact stiffness (K_n)	225
Tangential contact stiffness (K_t)	106
Coefficient of friction (μ)	0.5

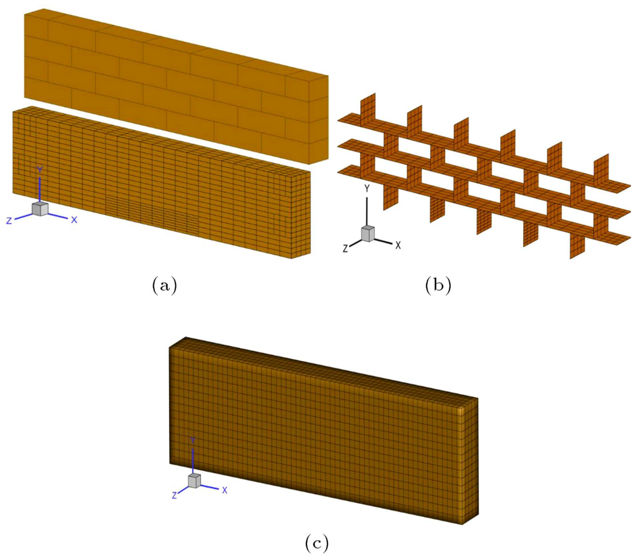

Figure 29. Numerical modeling: (a) Meso modeling: (b) interface element, and (c) macro modeling.

linearly before reaching the ultimate strength, and then lost the strength, and could no longer simulate the softening behavior Figure 30(c). This means that the linear behavior of the model continues and when the ultimate strength is reached, the sample fractured. Therefore, comparing the work done by Meso and the macro-method shows that the behavior represented by the macro-modeling is significantly different from reality. By comparing the amount of work done by each method, it can be seen that the amount of energy absorbed by the system in the macro modeling is significantly different from that in the experimental model (Eq. (7)):

$$W = F.d \text{ (N.m)}, \qquad W_{\text{exp}} = 2.85 \text{ (J)},$$

$$W_{\text{Meso}} = 2.38 \text{ (J)}, \qquad W_{\text{Macro}} = 0.64 \text{ (J)}. \tag{7}$$

According to Figure 31 the Meso method, the crack sites in the numerical and experimental models are in good agreement, however, in the macro model, the

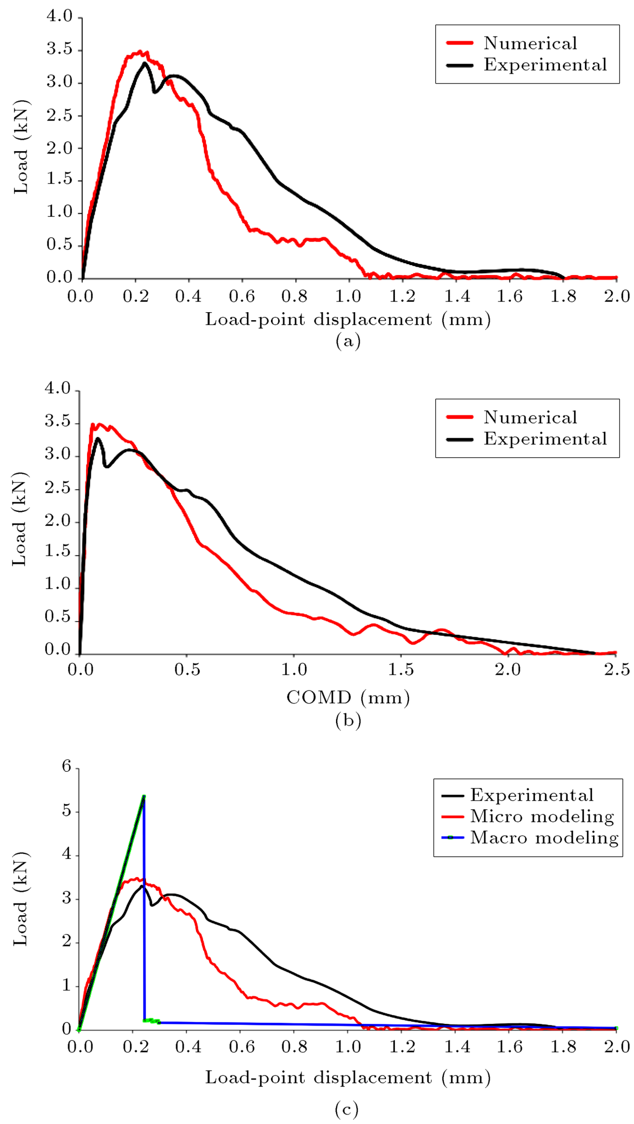

Figure 30. Comparison of numerical and experimental models: (a) The load-displacement graph of the numerical model using meso and experimental methods, (b) COMD using meso and experimental methods, and (c) the load-displacement graph of the numerical model using macro, meso, and experimental methods.

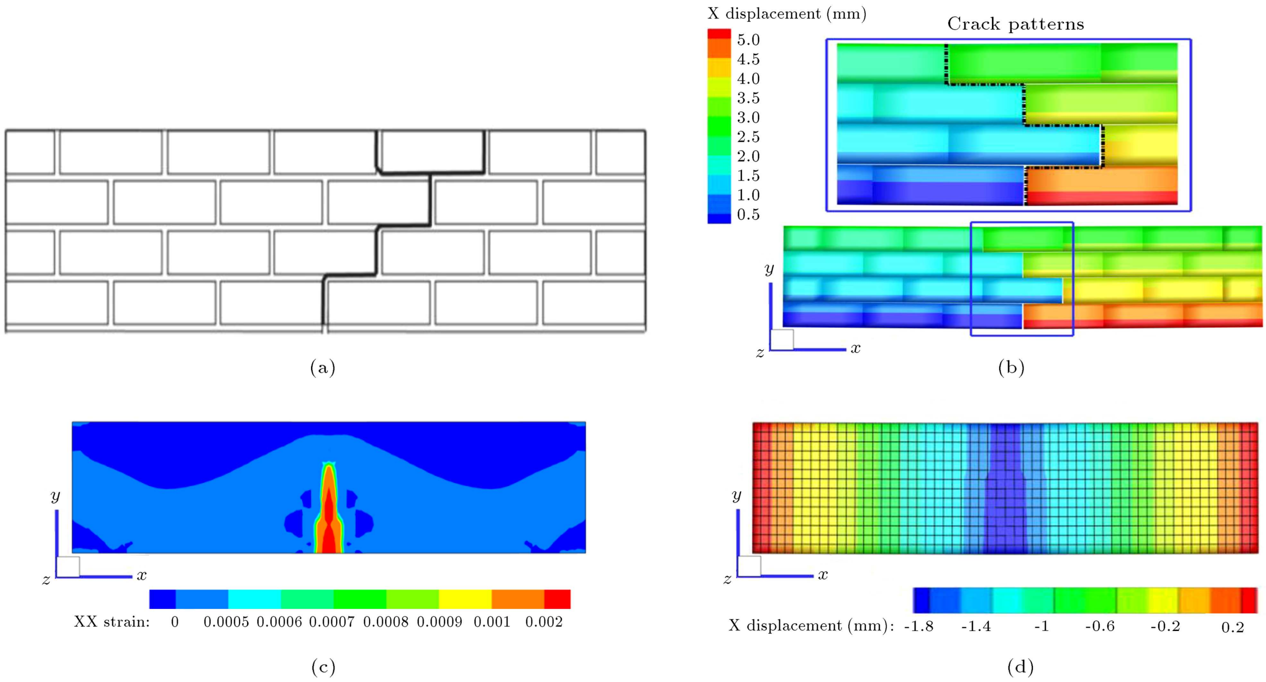

Figure 31. (a) Cracking pattern in the experimental model. (b) cracking and displacement pattern of the numerical model using meso method. (c) Displacement in numerical macro model. (d) Strain in the numerical macro model.

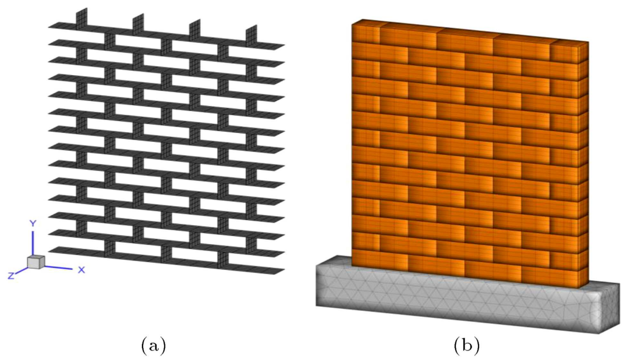

Figure 32. (a) Interface meshing and (b) brick wall and foundation meshing.

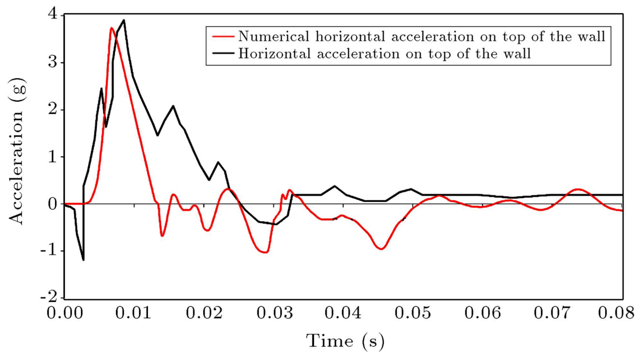

Figure 33. Comparison of time-acceleration in the cohesive-frictional interface constitutive model and experimental models.

midpoint of the sample is symmetrically affected by the plastic strain, which is far away from reality. The parameters listed in Table 5 were used for modeling the brick interface. The behavioral model of soil was the modified Mohr-Coulomb in terms of the topography of the zone. The soil model and its meshing were similar to those of the Model (4). Brick elements and interface meshing are shown in Figure 32. The comparison of the time-acceleration top of the wall between the numerical and experimental models shows that there is good agreement between the behavior of the numerical model and the experimental model (Figure 33). In addition, the comparison of the sliding position of the numerical model and the experimental model also shows that there is good agreement between them. In this case, the sliding occurred in the third and fourth bed joint rows. In fact, in the fourth bed joint row, a similar break occurred in the wall. Therefore, the amount of separation and sliding of the interface elements seems logical in Figure 34. The wall failure is a sliding failure [54], which usually occurs from the first few rows. To ensure the accuracy of the analysis, given the fact that the error rate in the numerical analysis was set to be $\varepsilon \leq 0.001$, the examination of the error value in each loading indicated that the error value and the maximum strain of plastic in each loading were proportional to each other (Figure 35). This is perfectly proportional to the amount of acceleration reaching the entire system (soil and wall). Then, the energy generated by the explosion is reduced and damped into the zone, giving the system elastic behavior. The number of iterations at each time step makes this problem very clear (Figure 36).

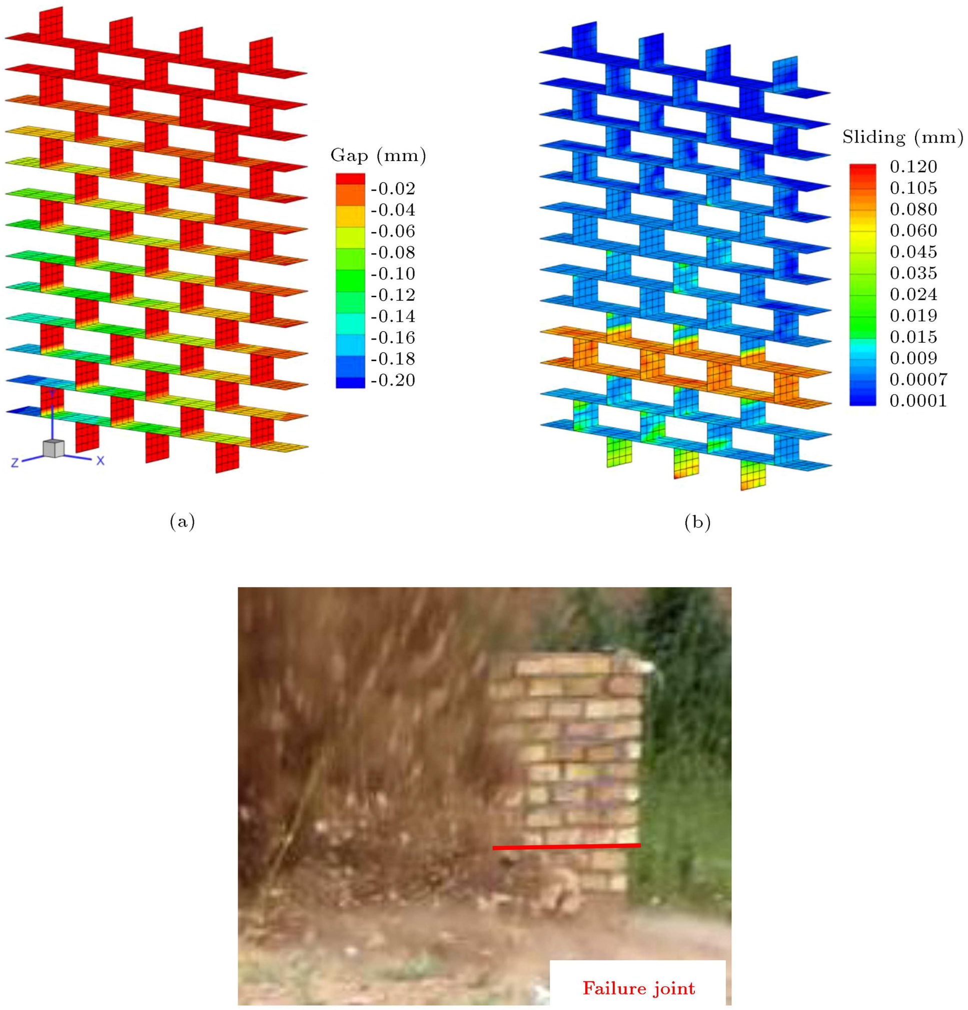

Figure 34. (a) Separation of interface elements, (b) sliding value of interface elements, and (c) slide in the fourth-bed joint row of the experimental model.

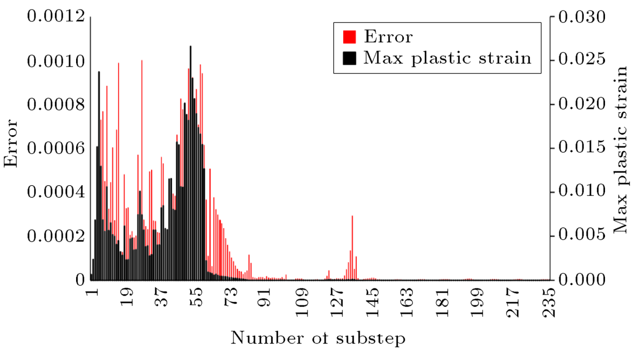

Figure 35. Comparison of the error rate and the maximum strain of plastic in each sub-step.

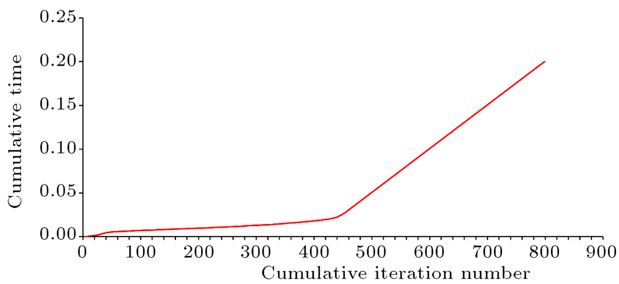

Figure 36. The cumulative time of analysis versus the number of cumulative iterations.

3.6. The first experimental model

After fixing all the parameters obtained from the numerical Model (2), the numerical model of Sample (1) is modeled with a value of 1.92 Kg TNT. This experiment was conducted in the same zone and there was almost no natural complication at a radius of 15000 mm around it. Hence, the zone is modeled smoothly in the numerical model. Additionally, the explosion crater and location of the explosives were not similar to those in the second experiment. Moreover, its shape was modeled numerically as excavated in the experiment site. The form of meshing and position of the crater with respect to the wall are shown in Figure 37. The numerical results of the Meso modeling

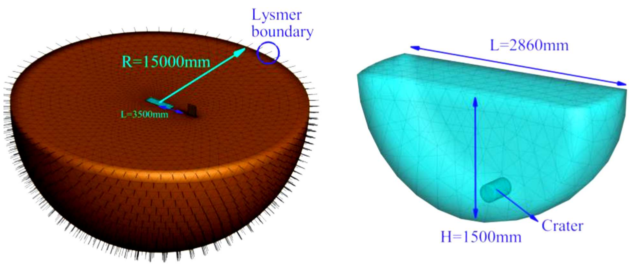

Figure 37. Numerical meso model and meshing.

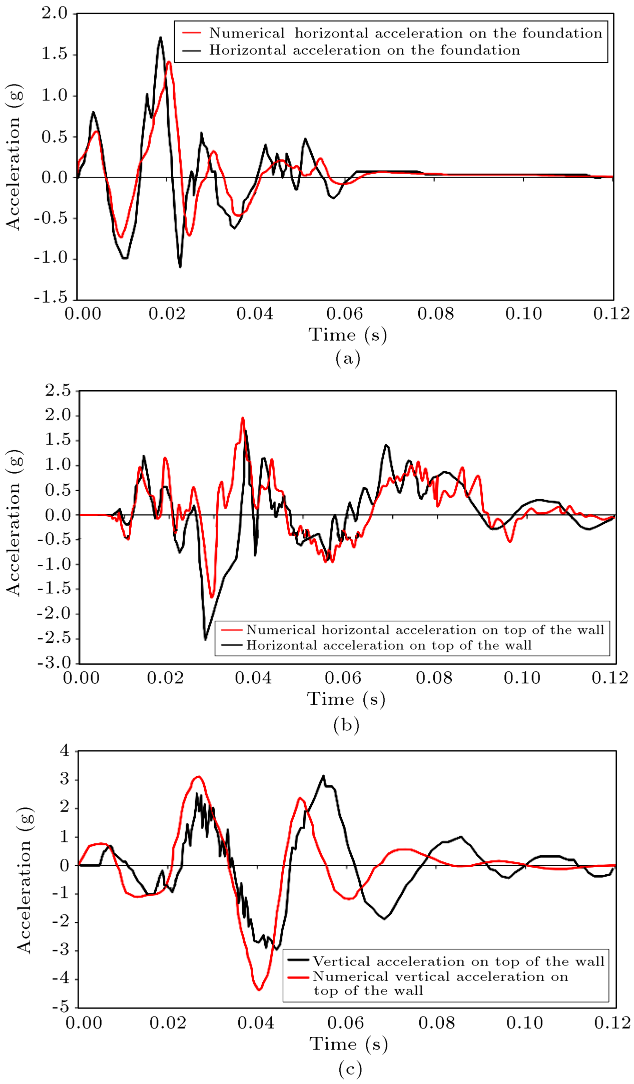

Figure 38. Comparison of the results of finite element and experimental models: (a) Horizontal acceleration on the foundation, (b) horizontal acceleration above the wall, and (c) vertical acceleration above the wall.

in the first experiment are shown with the equivalent value of 1.92 kg T.N.T in Figure 38. In the first experiment, besides the horizontal acceleration on the foundation, the vertical acceleration above the wall is also recorded. The comparison of the results of the numerical method and the experimental method shows that these modeling methods have quite appropriate consistency. It is worth noting that the behavior of the wall in this experiment was almost linear.

4. Conclusion

In this study, the behavior of the unreinforced masonry wall was investigated under high-frequency dynamic loads. Two unreinforced masonry walls were exposed to underground blasting. Then, there was an attempt to introduce the best numerical model which describes the behavior of the wall under high-frequency dynamic load:

- In the first model, the classic Drucker-Prager model was considered for soil and macro modeling was considered for masonry wall with free meshing. The maximum wall acceleration was predicted to be approximately appropriate. For the interconnection of the cracks, however, the numerical solutions were no longer close to the experimental behavior. The maximum response of numerical accelerations to the soil was also appropriate; however, the behavior became away from reality in the continuation, which is likely to be caused by the elastoplastic behavior of the soil as well as the topography of the site;
- In the second model, the soil parameters were fixed but the wall meshing was changed. Moreover, the dimensions of each wall element were changed to be as large as a brick, which makes the behavior of the wall more suitable than the previous model. It is possible since the wall fracture occurs within the mortar seams, and the larger elements cause the Gaussian integral points to be located closer to the location of the fracture and provide a more suitable behavior in reality;
- In the third and fourth model, because the soil and masonry wall parameters remained unchanged, the topography of the site became more realistic and the natural complications of the region were approximately modeled. This caused numerical responses to become closer to reality. As a result, the topography of the site is a major parameter in numerical modeling. In the following, by replacing the classic Drucker-Prager model failure criterion with the modified Mohr-Coulomb for the soil, it was observed that the responses are extremely close to reality. In this regard, the soil behavior in the numerical model improved due to the reduction of soil strength parameters after the first yield, and the actual situation is also the same;
- In the fourth model, since the soil behavior was considered in terms of the Mohr-Coulomb fracture surface, the topography of the site in the previous models nearly approached the experimental

behavior. Hence, the main focus was on the wall behavior. The masonry wall was modeled by using the frictional- cohesive zone material interface method, which is based on Traction-Displacement. The Menetrey-Willam failure criterion was also used for the behavior of the bricks, which can include softening in tension and compression. In this model, the parameters of the frictional-cohesive zone material were first validated. Then through the examination of the numerical model, it is observed that the experimental results were in good agreement with the numerical model. Therefore, this modeling method can be introduced as the most appropriate method for modeling the behavior of the walls, but more time is needed for the analysis of the computational costs in comparison to the other models. In this study, the general procedure to acheive the best numerical method to model the behavior of the soil and masonry wall under high-frequency dynamic loads was explained. This could serve as a guide for researchers to identify the process and method to achieve the most appropriate response.

References

1. Ali, S.S. and Page, A.W. "Finite element model for masonry subjected to concentrated loads", *Journal of Structural Engineering*, **114**(8), pp. 1761–1784 (1988).
2. Dhanasekar, M., Kleeman, P.W., and Page, A.W. "Biaxial stress-strain relations for brick masonry", *Journal of Structural Engineering*, **111**(5), pp. 1085–1100 (1985).
3. Andreaus, U. "Failure criteria for masonry panels under in-plane loading", *Journal of Structural Engineering*, **122**(1), pp. 37–46 (1996).
4. Ghiassi, B., Soltani, M., and Tasnimi, A.A. "A simplified model for analysis of unreinforced masonry shear walls under combined axial, shear and flexural loading", *Engineering Structures*, **42**, pp. 396–409 (2012).
5. Grande, E., Imbimbo, M., Rasulo, A., and Sacco, E. "A frame element model for the nonlinear analysis of FRP-strengthened masonry panels subjected to in-plane loads", *Advances in Materials Science and Engineering*, **2013**, 754162 (2013).
6. Berardi, V.P. "Initiation of failue for masonry subject to in-plane loads through micromechanics", *Modelling and Simulation in Engineering*, **2016**, 2959038 (2016).
7. Pantó, B., Calió, I., and Lourenço, P.B. "A 3D discrete macro-element for modelling the out-of-plane behaviour of infilled frame structures", *Engineering Structures*, **175**, pp. 371–385 (2018).
8. Choudhury, T., Milani, G., and Kaushik, H.B. "Experimental and numerical analyses of unreinforced masonry wall components and building", *Construction and Building Materials*, **257**, p. 119599 (2020).
9. Giambanco, G., Rizzo, S., and Spallino, R. "Numerical analysis of masonry structures via interface models", *Computer Methods in Applied Mechanics and Engineering*, **190**(49–50), pp. 6493–6511 (2001).
10. Chaimoon, K. and Attard, M.M. "Experimental and numerical investigation of masonry under three-point bending (in-plane)", *Engineering Structures*, **31**(1), pp. 103–112 (2009).
11. Akhaveissy, A.H. "The DSC model for the nonlinear analysis of in-plane loaded masonry structures", *The Open Civil Engineering Journal*, **6**(1) (2012).
12. Akhaveissy, A.H. "Lateral strength force of URM structures based on a constitutive model for interface element", *Latin American Journal of Solids and Structures*, **8**(4), pp. 445–461 (2011).
13. Akhaveissy, A.H. and Milani, G. "Pushover analysis of large scale unreinforced masonry structures by means of a fully 2D non-linear model", *Construction and Building Materials*, **41**, pp. 276–295 (2013).
14. Deng, M. and Yang, S. "Experimental and numerical evaluation of confined masonry walls retrofitted with engineered cementitious composites", *Engineering Structures*, **207**, p. 110249 (2020).
15. Khan, H.A., Nanda, R.P., and Das, D. "Numerical analysis of geosynthetic strengthened brick masonry panels", In *Advances in Structural Vibration*, Springer. pp. 35–41 (2020).
16. Karaton, M. and Çanskçi, K. "Investigation of head and bed mortar region effect in micro scale modelling of masonry walls", *Sigma: Journal of Engineering & Natural Sciences/Mühendislik ve Fen Bilimleri Dergisi*, **38**(2), pp. 741–756 (2020).
17. Komurcu, S. and Gedikli, A. "Macro and micro modeling of the unreinforced masonry shear walls", *European Journal of Engineering and Natural Sciences*, **3**(2), pp. 116–123 (2017).
18. Hao, H. and Wu, C. "Numerical study of characteristics of underground blast induced surface ground motion and their effect on above-ground structures. Part II. Effects on structural responses", *Soil Dynamics and Earthquake Engineering*, **25**(1), pp. 39–53 (2005).
19. Soheyli, M.R., Akhaveissy, A.H., and Mirhosseini, S.M. "Large-scale experimental and numerical study of blast acceleration created by close-in buried explosion on underground tunnel lining", *Shock and Vibration*, **2016**, 8918050 (2016).
20. Wu, C. and Hao, H. "Numerical study of characteristics of underground blast induced surface ground motion and their effect on above-ground structures. Part I. Ground motion characteristics", *Soil Dynamics and Earthquake Engineering*, **25**(1), pp. 27–38 (2005).
21. Ma, H.J., Quek, S.T., and Ang, K.K. "Soil-structure interaction effect from blast-induced horizontal and vertical ground vibration", *Engineering Structures*, **26**(12), pp. 1661–1675 (2004).

22. Ma, G. and Hao, H., and Zhou, Y. "Assessment of structure damage to blasting induced ground motions", *Engineering Structures*, **22**(10), pp. 1378–1389 (2000).

23. Shi, Y., Xiong, W., Li, Z.X., and Xu, Q. "Experimental studies on the local damage and fragments of unreinforced masonry walls under close-in explosions", *International Journal of Impact Engineering*, **90**, pp. 122–131 (2016).

24. Wang, J., Ren, H., Wu, X., and Cai, C. "Blast response of polymer-retrofitted masonry unit walls", *Composites Part B: Engineering*, **128**, pp. 174–181(2017).

25. Li, Z., Chen, L., Fang, Q., Chen, W., Hao, H., Zhu, R., and Zheng, K. "Experimental and numerical study on CFRP strip strengthened clay brick masonry walls subjected to vented gas explosions", *International Journal of Impact Engineering*, **129**, pp. 66–79 (2019).

26. Hu, X.D., Zhao, G.F., Deng, X.F., Hao, Y.F., Fan, L.F., Ma, G.W., and Zhao, J. "Application of the four-dimensional lattice spring model for blasting wave propagation around the underground rock cavern", *Tunnelling and Underground Space Technology*, **82**, pp. 135–147 (2018).

27. Ma, G.W., Hao, H., and Zhou, Y.X. "Modeling of wave propagation induced by underground explosion", *Computers and Geotechnics*, **22**(3–4), pp. 283–303 (1998).

28. ASTM, C. 109., *Standard Test Method for Compressive Strength of Hydraulic Cement Mortars (Using 2-in. or [50-mm] Cube Specimens)*: ASTM International (2013).

29. Committee, M.S.J. "Building code requirements for masonry structures (TMS 402-11/ACI 530-11/ASCE 5-11)", The Masonry Society, Boulder, CO. (2011).

30. ASTM Committee D-18., *Standard Test Method for Consolidated Undrained Triaxial Compression Test for Cohesive Soils*: ASTM International (2011).

31. ASTM. D. 3080., *Standard Test Method for Direct Shear Test of Soils Under Consolidated Drained Conditions*, ASTM West Conshohocken (2011),

32. Goel, R.K. and Chopra, A.K. "Evaluation of modal and FEMA pushover analyses: SAC buildings", *Earthquake Spectra*, **20**(1), pp. 225–254 (2004).

33. Lysmer, J. and Kuhlemeyer, R.L. "Finite dynamic model for infinite media", *Journal of the Engineering Mechanics Division*, **95**(4), pp. 859–878 (1969).

34. Liu, G.R. and Achenbach, J.D. "A strip element method for stress analysis of anisotropic linearly elastic solids", *Journal of Applied Mechanics*, **61**(2), pp. 270–277 (1994).

35. Gratkowski, S., Pichon, L., and Razek, A. "Infinite elements for 2D unbonded wave problems", COMPEL, - *The International Journal for Computation and Mathematics in Electrical and Electronic Engineering*, **14**(4), pp. 65–69 (1995).

36. Chen, S.G., Cai, J.G., Zhao, J., and Zhou, Y.X. "Discrete element modelling of an underground explosion in a jointed rock mass", *Geotechnical & Geological Engineering*, **18**(2), pp. 59–78 (2000).

37. Jiao, Y.Y., Zhang, X.L., Zhao, J., and Liu, Q.S. "Viscous boundary of DDA for modeling stress wave propagation in jointed rock", *International Journal of Rock Mechanics and Mining Sciences* (1997), **44**(7), pp. 1070–1076 (2007).

38. Army, U.S., *Structures to Resist the Effects of Accidental Explosions*, US Government Printing Office (1969).

39. Station, U.A. TM5-855-1, *Fundamentals of Protective Design for Conventional Weapons*, US Army (1986).

40. Murrell, D.W. and Joachim, C.E., *Singapore Ground Shock Test*, Engineer Research and Development Center Vicksburg Ms Structures Lab. (1996)

41. Fan, S.C., Jiao, Y.Y., and Zhao, J. "On modelling of incident boundary for wave propagation in jointed rock masses using discrete element method", *Computers and Geotechnics*, **31**(1), pp. 57–66 (2004).

42. Willam, K.J. "Constitutive model for the triaxial behavior of concrete", *International Association for Bridge and Structural Engineering Proceedings*, **19**, pp. 1–30 (1975).

43. Thompson, M.K. and Thompson, J.M., *ANSYS Mechanical APDL for Finite Element Analysis*, Butterworth-Heinemann (2017).

44. Asteris, P.G. and Antoniou, S.T. "Mathematical macromodeling of infilled frames: State of the art", *Journal of Structural Engineering*, **137**(12), pp. 1508–1517 (2011).

45. Madan, A., Reinhorn, A.M., Mander, J.B., and Valles, R.E. "Modeling of masonry infill panels for structural analysis", *Journal of Structural Engineering*, **123**(10), pp. 1295–1302 (1997).

46. Milani, G. and Tralli, A. "A simple meso-macro model based on SQP for the non-linear analysis of masonry double curvature structures", *International Journal of Solids and Structures*, **49**(5), pp. 808–834 (2012).

47. Wood, D.M., *Soil Behaviour and Critical State Soil Mechanics*, Cambridge University Press (1990).

48. Bićanić, N. "Detection of multiple active yield conditions for Mohr-Coulomb elasto-plasticity", *Computers & Structures*, **62**(1), pp. 51–61(1997).

49. Menetrey, P. and Willam, K.J. "Triaxial failure criterion for concrete and its generalization", *Structural Journal*, **92**(3), pp. 311–318 (1995).

50. Alfano, G. and Sacco, E. "Combining interface damage and friction in a cohesive-zone model", *International Journal for Numerical Methods in Engineering*, **68**(5), pp. 542–582 (2006).

51. Giambanco, G., Rizzo, S., and Spallino, R. "Numerical analysis of masonry structures via interface models", *Computer Methods in Applied Mechanics and Engineering*, **190**(49), pp. 6493–6511 (2001).

52. Parrinello, F., Failla, B., and Borino, G. "Cohesive-frictional interface constitutive model", *International Journal of Solids and Structures*, **46**(13), pp. 2680–2692 (2009).

53. Vandoren, B., De Proft, K., Simone, A., and Sluys, L.J. "Mesoscopic modelling of masonry using weak and strong discontinuities", *Computer Methods in Applied Mechanics and Engineering*, **255**, pp. 167–182 (2013).

54. Boussabah, L. and Bruneau, M. "Review of the seismic performance of unreinforced masonry walls", In *Proc. of the 10th World Conf. on Eq. Eng.* (1992).

Biographies

Amir Houshang Akhaveissy is an Associate Professor in Civil Engineering. He was a member of the faculty of the Razi University for more than 15 years, with more than 20 years of teaching experience in different fields, more focusing on finite elements. Moreover, he has more than 30 national and international published papers, mainly on the behavior of masonry buildings, in reputed journals such as the Journal of Structural Engineering, and Mechanical Science.

Ali Permanoon is a PhD student in Civil Engineering at the Razi University of Iran. His master thesis was about masonry walls and the evaluation of the effect of underground waves on the masonry building and walls. The subject of his thesis is a numerical study on a concrete fracture on meso scale; he published at least 5 papers related to this issue. His interests include fracture mechanics, finite element analysis, and analysis of the behavior of masonry buildings. He published some articles in national and international papers in reputed journals.

Roya Raeisi is a PhD student in Civil Engineering at the Bu-Ali Sina University of Iran. Her interests include fracture mechanics and finite element analysis. She received her master degree from the Razi University of Iran. The subject of her master dissertation was the effects of prestressing resulting from welding on the resistance of steel frames. The subject of her thesis is a numerical and experimental study on preplaced aggregate concrete. She published some articles in the national and international reputed journals.